CHARGE SCREENING OF 2-DIMENSIONAL HYBRID ORGANIC-INORGANIC

PEROVSKITES

A Thesis

by

MOHAMMED SHYIKH

Submitted to the Graduate and Professional School of
Texas A&M University
in partial fulfillment of the requirements for the degree of

MASTER OF SCIENCE

Chair of Committee,   Qing Tu
Committee Members,   Xiaofeng Qian
                      Zi Jing Wong
Head of Department,   Ibrahim Karaman

December 2021

Major Subject: Materials Science and Engineering

Copyright 2021 Mohammed Shyikh

ABSTRACT

Hybrid organic-inorganic perovskites have drawn much attention over the past decade because of their excellent electrical properties, which have allowed for their implementation in photovoltaics, optoelectronics, and other device applications. Within the broader class of hybrid organic-inorganic perovskites, there are subclasses based on the dimensionality and structure of the perovskite material. One notable subclass is the 2 dimensional Ruddlesden-Popper perovskite family. 2D Ruddlesden-Popper perovskites exhibit high quantum confinement due to their layered quantum well structure. The 2D Ruddlesden-Popper phase perovskites have also drawn significant attention due to their superior ambient stability compared to their 3D counterpart. The broad 2D class of semiconducting materials have also garnered much intrigue since the discovery of graphene for ultra-thin devices with exceptional performance. One bottleneck to increasing the efficiency of 2D semiconducting material and perovskite based devices is non-radiative recombination losses and charge scattering caused by defects and charge perturbations at contact interfaces. In this work, I identify an effective methodology which can be used to study the charge screening behaviors of 2D Ruddlesden-Popper perovskites. Using kelvin probe force microscopy, the surface potential, which is affected by charge transfer and perturbations, can be mapped for 2D perovskite samples of various thicknesses thereby giving insights to the charge screening lengths of the various perovskite materials. This work investigates the charge screening behavior of C4n1, C4n2, C4n3, and C4n5 2D perovskites. Results show trends of increasing charge screening behavior with layer number for each perovskite sample. Furthermore, it is shown that higher n-number 2D perovskite samples are more effective at screening charge perturbations compared to the low n-number perovskites. Overcoming the hurdle of charge transfer efficiency losses due to charge perturbations at interfaces is crucial to enabling the engineering of more efficient perovskite devices. Future studies using this methodology can be used to identify how charge screening behavior depends on the organic ligands of various 2D perovskites.

DEDICATION

To my beloved mother, father, and brother for all of their sacrifice, unending love, and

everlasting support.

ACKNOWLEDGEMENTS

CONTRIBUTORS AND FUNDING SOURCES

Contributors

This work was supervised by a thesis committee consisting of Professors Qing Tu and Xiaofeng Qian of the Department of Materials Science and Engineering and Professor Zi Jing Wong of the Department of Aerospace Engineering.

2-Dimensional Hybrid Organic-Inorganic Perovskites used in the experiments were synthesized by Dr. Ioannis D. Spanopoulos of Northwestern University and by Doyun Kim of the Tu research group in the Materials Science and Engineering department of Texas A&M University.

All other work conducted for the thesis was completed by the student independently.

Funding Sources

NOMENCLATURE

HOIP	Hybrid Organic-Inorganic Perovskite
LED	Light Emitting Diode
RP	Ruddlesden-Popper
AFM	Atomic Force Microscopy
KPFM	Kelvin Probe Force Microscopy
E_g	Electronic Band Gap
E_{VAC}	Vacuum Level
E_F	Fermi Level
CBM	Conduction Band Minimum
VBM	Valence Band Maximum
EA	Electron Affinity
IE	Ionization Energy
WF	Work Function
3D	Three Dimensional
2D	Two Dimensional
$MAPbI_3$	Methylammonium Lead Iodide
SKPM	Scanning Kelvin Probe Microscopy
EFM	Electrostatic Force Microscopy
C4n1	Butylammonium Lead Iodide 2D Perovskite $(BA)_2PbI_3$
C4n2	$(BA)_2(MA)_1Pb_2I_7$ 2D perovskite
C4n3	$(BA)_2(MA)_2Pb_3I_{10}$ 2D perovskite
C4n5	$(BA)_2(MA)_4Pb_5I_{16}$ 2D perovskite

XRD   X-Ray Diffraction

CPD   Contact Potential Difference

TABLE OF CONTENTS

LIST OF FIGURES

LIST OF TABLES

1. INTRODUCTION

Hybrid Organic-Inorganic Perovskites (HOIPs) are a class of materials which exhibit extraordinary optical and electrical characteristics, namely, broad light absorption spectra[1], tunable band gaps[2], high charge carrier mobility[3], and long carrier lifetimes[4]. These materials have also displayed a high level of tunability based on the HOIP chemical composition, dimensionality, and doping[5-6]. These properties make HOIPs extremely versatile materials and allow for their incorporation in a plethora of device applications such as, solar cells[7], light-emitting diodes (LEDs)[8], transistors[9], lasers[10], and photodetectors[11]. Within just a decade of research and development, perovskite photovoltaics have surpassed conventional silicon photovoltaics achieving power-conversion efficiencies of 25.5% and tandem perovskite solar cells achieving 29.5%[12]. Despite these impressive advances, one limiting factor for HOIP-based devices is non radiative recombination losses and charge carrier scattering due to defects within the HOIP materials and at contact interfaces with other materials[13]. Additionally, charge perturbations due to impurities at contact interfaces are known to negatively affect carrier mobility in graphene-SiO2 interfaces[14]. To this end, exploring the charge screening capabilities of HOIPs for the sake of defect and charge perturbation passivation becomes an imperative field of study. Understanding the charge screening behaviors of HOIPs may enable the engineering of smaller and more efficient HOIP devices in their wide variety of applications.

1.1 OBJECTIVES

While perovskites display incredible properties, one bottleneck to the engineering of efficient nano-scale devices is charge perturbation induced carrier scattering. The charge perturbation screening behaviors, specifically the screening lengths, of 2-Dimensional Ruddlesden

Popper (RP) perovskites remains largely unknown. The objective of this study is to unveil the charge screening behaviors of 2D RP perovskites with the general formula $(BA)_2A_{n-1}B_nX_{3n+1}$ while varying the quantum well number of the perovskites (n = 1, 2, 3, and 5). This is accomplished by employing kelvin probe force microscopy (KPFM) to monitor how the 2D RP perovskite surface potential changes as the layer number of the investigated perovskite flakes increases. This work serves to elucidate two main points: 1) The charge screening behaviors of the specific perovskite materials being investigated and 2) How changing the quantum well number of these perovskites influences those charge screening behaviors. In the future, this may enable 2D perovskite based devices with improved efficiencies in a variety of applications.

1.2 LIMITATIONS

The formulation of this study's research goals is quite specific. To further shed light on the charge screening properties of 2D perovskites, the methodology used herein can be applied to investigate the effect of the organic spacer molecule on the charge screening properties. However, this study does show the efficacy of the technique used and details the methodology which can easily be applied to study other structural influences of perovskites on their charge screening properties.

1.3 ORGANIZATION OF THIS STUDY

This study is organized into 5 sections: the introduction, background information, materials and methods, results and discussion, and finally, the conclusion. The introduction aims to give a

brief overview of the significance of this study and how it is conducted. It also details the objectives of the study, its limitations, and the organization of the summarized work. The background section presents detailed information on semiconductor properties with a focus on defects and their influence on carrier mobilities, electrical characteristics, charge screening effects, HOIP structure and dimensionality, AFM and KPFM, and a literature review of charge screening studies conducted on perovskites and other 2D materials. This section lays the necessary foundation for understanding the methodology and interpreting the results of the study. The methods and materials section introduces the exact materials and their structures used in this research, briefly overviewing their synthesis and characteristics, then goes into the preparation of the samples used in the experiments and the methodologies for data gathering and analysis. This is followed by the results and discussions section which presents the main findings of this research and discusses the significance of these findings. Finally, the conclusion section summarizes the work and proposes future studies that may follow from it.

2. BACKGROUND

2.1 SEMICONDUCTOR FUNDAMENTALS

Semiconductors display intermediate conductivities between that of metals and insulators generally in the range of 10^{-6} to $10^4 \frac{\Omega}{m}$[15]. In conductive and semiconducting materials, an important property is the charge carrier mobility. This carrier mobility defines the ease with which charge carriers can move through a crystal lattice. In an ideal crystal, when an electric field is applied, electrons will accelerate indefinitely in a direction opposite to that of the electric field due to their negative electric charge[15]. However, in real materials there does exist some constant current that is achieved over time when an external bias is applied. This constant current, which is the limitation to the charge carrier acceleration is indicative of certain forces that exist which limit charge carrier

mobility in real crystals. These forces counter the charge carrier acceleration and result from the scattering of charge carriers from various lattice defects. These defects are manifested in a crystal as impurity atoms, interstitial atoms, vacancies, thermal vibrations of lattice atoms (phonons) and dislocations. All of these defects serve to hinder the path of charge carriers, depleting their kinetic energy with every scattering event. Although there are scattering events, charge carriers will still have a net movement based on the applied electric field. This net movement is known as the drift velocity of the charge carriers. The drift velocity is defined by the strength of the electric field and the frequency of the scattering events which is known as the charge carrier mobility. For example, the drift velocity of an electron can be denoted by equation 1.

$$v_d = \mu_e E \tag{1}$$
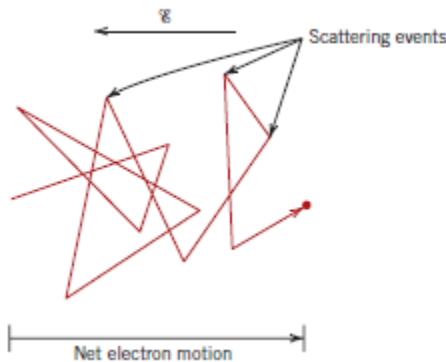
Figure 1: Depiction of scattering events encountered by an electron in an applied electric field[15].

There are many factors that can influence the charge carrier mobilities of semiconducting materials. Two of these factors are impurity content and temperature. Semiconductor materials can intrinsic or extrinsic semiconductors. Silicon, germanium, and some compound materials display intrinsic semiconduction. Intrinsic semiconductors are semiconductors in which their semiconducting behavior is based on the inherent electronic properties of the materials themselves.

4

In contrast, extrinsic semiconductors are those whose electrical behaviors are dictated primarily by external impurity atoms known as dopants. Dopant atoms introduce additional charge carriers into the lattice that can engage in conduction. P-type dopants introduce more holes and n-type dopants introduce more free electrons. The concentration of dopant atoms influences the carrier mobility as these impurities increase the probability of scattering events occurring. As for temperature dependency, there is a competition between enhanced kinetic energy available to the charge carriers and enhanced probability for scattering events to occur given that thermal scattering increases with rising temperature. In general, the mobility which defines the frequency of scattering events decreases with increasing temperature.

2.2 ELECTRONIC ENERGY LEVELS AND METAL SEMICONDUCTOR CONTACT

In discussing charge screening, it is imperative to understand the effect that interfaces have on the electronic structure of the semiconducting materials. These effects can be understood by looking at how the electronic energy levels of the semiconductor are affected by contact at the interface. Doping, the type of contacting material, and the morphology and crystal orientation of the semiconducting material all influence the electronic band structure and thereby the degree of so called band-bending at interfaces between the semiconductor and other materials.

We begin this discussion with a formulation of energy band structures in solids. For any atom, there are specific energy levels which may be occupied by electrons. These discrete energy levels are described by shells (n=1,2,3…) and subshells (*s*, *p*, *d*, and *f*) which are occupied by the electrons. The electrons are arranged in the shells in accordance with the Pauli exclusion principle filling the subshell levels with 2 electrons per subshell containing opposite spins. This is the arrangement of isolated atoms. As atoms of a solid coalesce into a continuous solid forming

covalent bonds and decreasing the interatomic separation, the discrete energy levels described by atomic orbitals are perturbed and split into closely packed electronic states. The distance between each energy level of a solid is very small and as such, the electronic structure of continuous solids is effectively described by bands of these very closely packed energy levels.
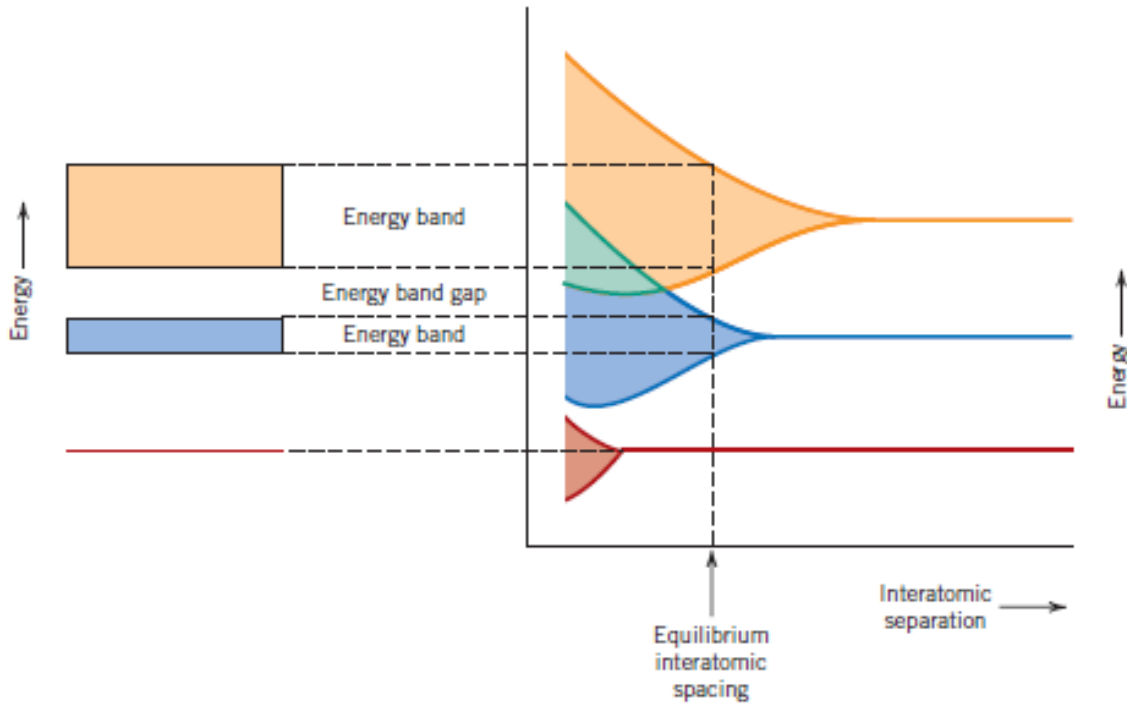
Figure 2: Schematic representation of electronic band structure as a function of decreasing interatomic separation causing the formation of electronic bands[16].

The formulation of the energy band structure of semiconductors allows for defining parameters which are critical to fundamentally understanding conductive materials and their interfaces. These parameters are depicted in figure 3; they are the energy band gap (E_g), vacuum level (E_{vac}), fermi level (E_F), conduction band minimum (CBM), valence band maximum (VBM), electron affinity (EA), ionization energy (IE) and work function (WF). The electronic band structures of materials and thus their associated band parameters can vary based on various internal and external factors.

For example, materials purity or doping concentration, crystallographic structure and surface orientation, surface morphology or roughness, and surface contamination can all affect the electronic parameters of conductive materials[17]. The conduction and valence bands are essentially the electron and hole transport levels respectively in semiconductors. The electronic band gap is the energy difference between the CBM and the VBM. This bandgap defines the energy required for electrons in the valence band to be promoted and participate in conduction in the conduction band. E_{VAC} is defined as the energy level of a stationary electron (no kinetic energy) positioned right outside of the surface of the material. This is essentially a reference state for the other energy levels of charge carriers in the semiconductor. The EA and IE of charge carriers can be defined relative to the E_{VAC} as the difference between it and the CBM and VBM respectively. Thus, the IE can be understood as the energy necessary to remove an electron from the system, considering that most electrons in an undoped or not excited system will contain the majority of electrons near the VBM. Similarly, the EA is the energy gained by an electron taking it from the vacuum level into the CBM.
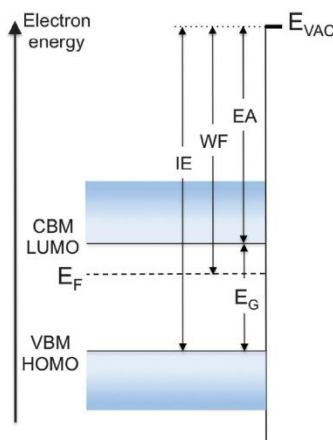
Figure 3: Energy level diagram depicting important electronic band structure parameters[17].

The parameter most important to this study is the WF. This is the property that can be probed by KPFM. The work function is defined as the difference between the vacuum level and the fermi level of the semiconductor. The fermi level in metals is the boundary between occupied and unoccupied states. For semiconductors, the fermi level is a statistical value defined by the Fermi-Dirac distribution which falls between the CBM and the VBM for non-degenerate semiconductors. The WF can be understood as the energy barrier for electrons at the fermi level to escape to the vacuum level i.e., escaping the solid. The work function of a material has two contributing components, a bulk component and a surface component. The bulk component of the work function depends on the electron density and density of states in the material. Density of states defines the proportion of occupied states at specific system energies. The surface component has an additional arising from the redistribution of charges at the surfaces of solids which are a result of crystallographic orientation of atoms at the surface of the material[17].

2.3 ELECTRIC FIELD SCREENING

Electric field screening, also known as charge screening, is an essential effect to understand in thin materials such as 2-dimensional materials. Charge screening determines the effectiveness with which substrate and interlayer interactions affects the electronic properties of the materials in device applications. Additionally, defects introduced at interfaces in materials act as scattering centers which can bottleneck device performance. One crucial parameter to understand with regards to charge screening is the charge screening length. At the charge screening length, electrical perturbations from the substrate charge transfer doping, interlayer effects, and defects are completely screened. Thus, at this length, device performance is expected to be optimized while active material thinness is miniaturized yielding highly efficient ultra-thin devices.

2.4 HYBRID ORGANIC-INORGANIC PEROVSKITES

Perovskites are a large class of materials having the same crystallographic structure as prototypical perovskite calcium titanate ($CaTiO_3$). This ABX_3 structure is known as the perovskite structure in which A and B are cations and X is an anion. Ideally, perovskite materials consist of a perfect cubic structure consisting of corner-sharing BX_6 octahedra. In this ideal structure, the B-X-B bond angle is 180° and the A cations inhabit the interstitial sites[18]. However, lattice distortions which are deviations from the ideal crystal structure can occur based on the ions used in the perovskite structure. These deviations can also be caused by phase transitions into the lower symmetry orthorhombic and tetragonal phases at lower temperatures[19-20]. The Goldschmidt tolerance factor describes the distortion of perovskite structures and their stability for different ions in the structure[21]. The Goldschmidt tolerance factor is given by equation 2 where r_A and r_B are the A and B-site cationic radii respectively and r_X is the anionic radius. The Goldschmidt tolerance factor can be interpreted by its numerical value, for example, t=1 indicates a perfectly stable perovskite structure. A t value between 0.8 and 1 perovskites will generally form, and t value greater than 1 indicates that the A site cation is too large relative to the other ions and a stable perovskite will not form[22].

$$t = \frac{r_A + r_X}{\sqrt{2}(r_B + r_X)} \tag{2}$$
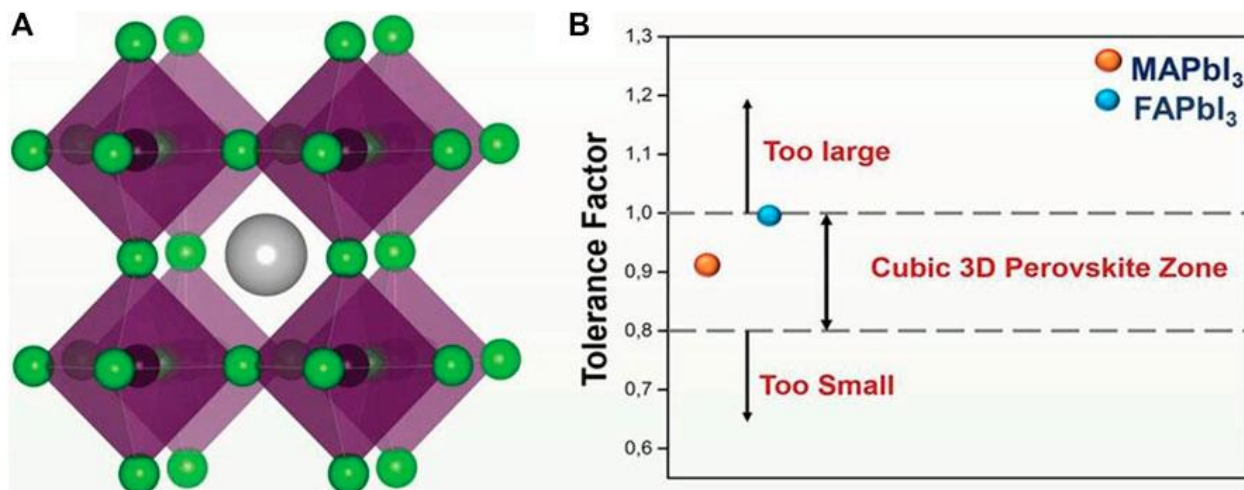
Figure 4: (a) ABX_3 perovskite lattice depiction where the x anions are shown in green, the B cations are shown in black at the center of the BX_6 octahedra, and the A cation is shown in grey. (b) Goldschmidt tolerance factor graph depicting the tolerance factors of two common HOIPs[23].

So far the structure mentioned pertains to 3-dimensional perovskite structures in which the ABX_3 lattice depicted in Figure 4a is tessellated throughout the volume of the crystal in every direction. Additionally, the prototypical calcium titanate is an example of an inorganic perovskite. The perovskite subcategory that has garnered much interest because of their rise in photovoltaic performance are hybrid organic-inorganic perovskites (HOIPs). 3-dimensional HOIPs adopt the same ABX_3 crystal structure but consist of an organic monovalent A-site cation (for example, $CH_3NH_3^+$), a divalent B-site metal cation (for example, Sn^{2+} or Pb^{2+}), and halide X-site anions (for example, I^- or Br^-). The crystal structure of these 3D HOIPs consists of corner-sharing BX_6^{4-} octahedra with the organic A cations filling the interstitial sites. 3D HOIPs such as the prototypical methylammonium lead iodide ($MAPbI_3$) have shown outstanding characteristics, however, display an inherent instability to moisture and prolonged light exposure[24-34].

10

For this reason, lower dimensional 2D HOIPs have been engineered which have a layered quantum well structure which are formed by layers of BX_6^{4-} octahedra sandwiched between organic ligands. These 2D perovskites, and namely the Ruddlesden-Popper (RP) type perovskites have garnered increasing attention due to their superior ambient stability[35]. The general formula of these RP HOIPs is $(RNH_3)_2A_{n-1}B_nX_{3n+1}$ (n = 1,2,3,...), where RNH_3 is a linear or aromatic alkylammonium cation sandwiching the inorganic layers and n indicates the number of BX_6^{4-} octahedral layers within each quantum well. In these materials, the hydrophobic organic layers protect the inorganic layers from moisture in ambient air leading to higher stability compared to the 3D analogue[36-39].
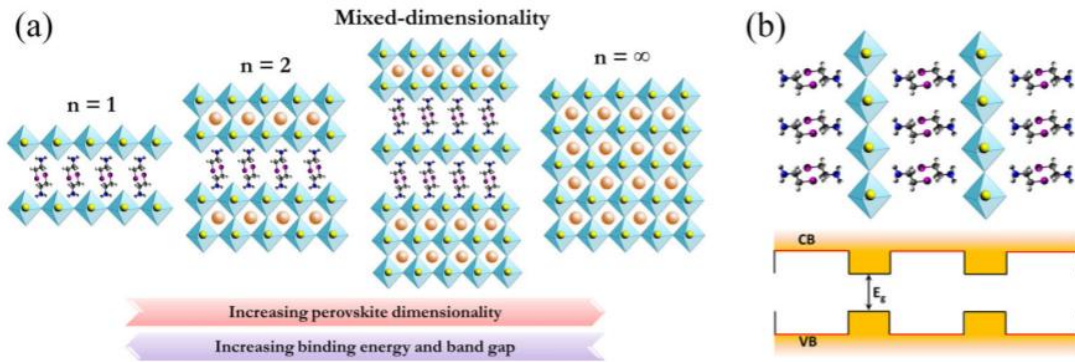
Figure 5: (a) Diagram depicting perovskite dimensionality showing inorganic layers with different thicknesses up to the 3D conformation. (b) Depiction of the stacked quantum well structure of 2D RP perovskites[40].

The quantum well electronic structure of these 2D RP perovskites implies quantum confinement of charge carriers along one dimension. This quantum confinement occurs as a result of dielectric organic layers inhibiting charge transport between inorganic layers. Furthermore, the

electronic properties of these 2D perovskites can be easily tuned by varying the type of organic dielectric used and the number of inorganic layers, n[41].

2.5 ATOMIC FORCE MICROSCOPY AND KELVIN PROBE FORCE MICROSCOPY

The primary techniques used in this study are scanning probe microscopy based techniques. Atomic force microscopy (AFM) is an extremely versatile and powerful technique in probing the nanoscale properties of materials. AFM is a scanning probe based technique using a probe with an extremely small contact radius, usually in the tens of nanometer range, to measure sample topography and properties with nanometer resolution. There are multiple basic operational AFM modes. The primary function of AFM is to determine sample topography. This can be done in contact or tapping modes. AFMs can also be used to measure force spectra of materials which can yield information on the Young's modulus and other mechanical properties of materials[42]. Functional modes of AFM exist which extend the capabilities of the base modes to measure electrical[43], thermal[44], magnetic[45], and a whole suit of other material properties[46].
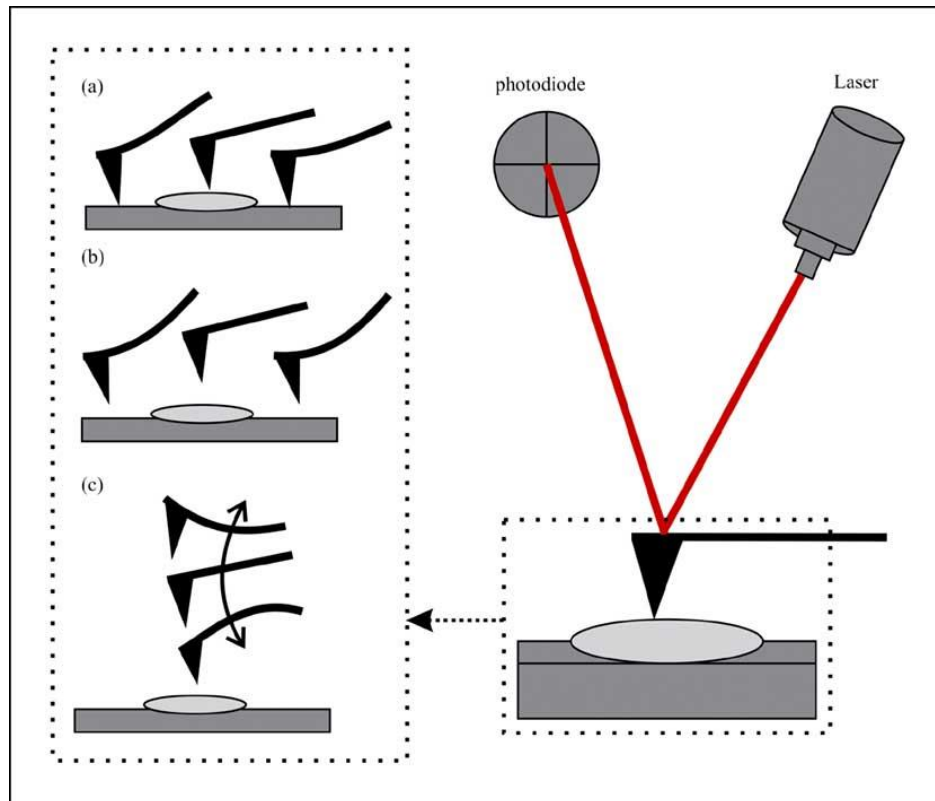
Figure 6: Depiction of basic AFM modes (a) contact (b) non-contact (c) tapping[47].

The basic topography modes of AFM include contact and tapping modes. Contact mode AFM involves "dragging" the AFM tip across the sample surface to determine the sample topography. The detection method used by AFMs involves using a laser deflected off the probe onto a photodiode which induces a voltage based on the reflected laser spot's position on the diode. Initially, the laser spot is adjusted so as to produce a 0 voltage on the center of the photodiode. Then as the tip is brought into contact with the sample, the physical deflection of the probe translates to a shift in the laser spot's position on the photodiode which produces a voltage. A setpoint voltage is then defined by the user which the AFM feedback loop uses to readjust the cantilever deflection via piezoelectric actuators which control the stage height. In contact mode, as the tip traces the sample surface and encounters high or low features, the piezoelectric actuator

readjusts the probe deflection using the setpoint voltage and the feedback loop. Depending on the voltage required to readjust the tip position, the sample topography is traced in real time as it raster scans over the sample surface area. Contact mode AFM may erode the tip of the AFM probe over time if a durable probe such as a diamond or diamond like carbon probe isn't used.

Tapping mode is more typically used for looking at sample topography than contact mode. In contrast to contact mode, tapping mode AFM involves the AFM probe intermittently coming into contact with the sample surface which preserves the sharpness of the tip and thereby the resolution of the AFM. The tip is vibrated at it's resonance frequency and the oscillation amplitude of the AFM probe is detected instead of the constant deflection in contact mode. The resonance frequency of the probe can be found by sweeping through a range of frequencies and detecting the oscillation amplitude. As the tip raster scans across the sample surface, and encounters high and low features, the oscillation amplitude of the AFM probe changes. A feedback loop is also used in this mode to readjust the probes oscillation to the setpoint amplitude.

The functional mode of AFM used in this research is kelvin probe force microscopy (KPFM). KPFM, also known as scanning kelvin probe microscopy (SKPM), is based on the macroscopic kelvin probe method to investigate surface potentials. In dual-pass KPFM, the first pass over the sample is used to scan the topography on a single scan line. Then the second pass is used to map the surface potential by lifting the probe above the sample surface at a predefined height above the sample. The first pass is typically done in tapping mode using a piezoelectric element to mechanically oscillate the probe at its resonance frequency. During the KPFM pass, the probe is electrically driven (no mechanical oscillation via piezo element) using an applied bias.
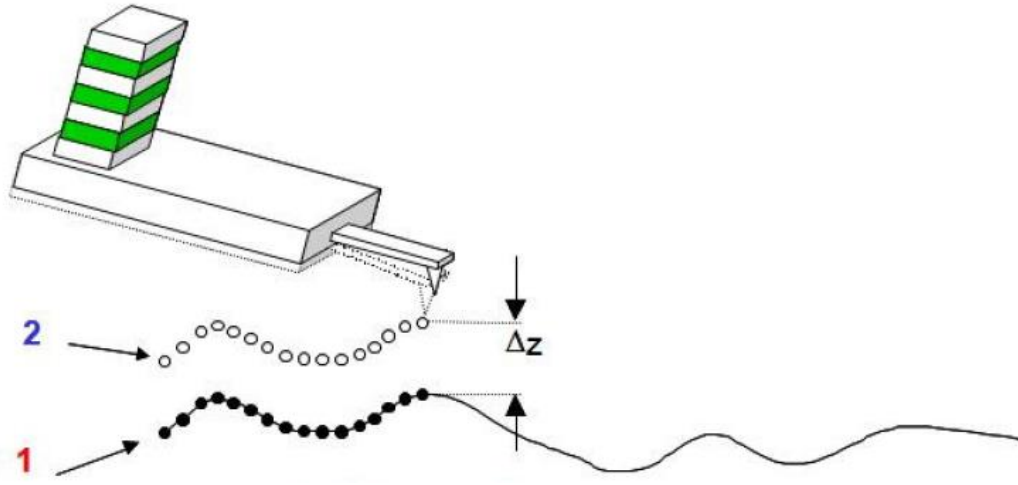
Figure 7: Schematic showing the two passes in KPFM, 1 being the topography scan, and 2 being the subsequent KPFM scan at a lifted height above the sample[48].

This voltage difference between the tip and the sample is the difference between the difference between any DC component of the applied bias and the surface potential summed with the AC component of the applied bias.

$$V = (V_{DC} - V_s) + V_{AC} \sin \omega t \qquad (3)$$

We can also describe the tip-sample system as a parallel plate capacitor in which the capacitive force is proportional to the gradient of capacitance and the square of the applied potential as described in equation 4.

$$F = \frac{1}{2} \frac{\partial C}{\partial z} V^2 \qquad (4)$$

Thus, substituting equation 3 into equation 4 with some algebraic manipulation we arrive at an equation modeling the tip sample capacitive force shown in equation 5[48].

$$F = \frac{1}{2} \frac{\partial C}{\partial z} \left(\left[(V_{DC} - V_s)^2 + \frac{1}{2} V_{AC}^2 \right] + 2[(V_{DC} - V_s)V_{AC} \sin(\omega t)] - \left[\frac{1}{2} V_{AC}^2 \cos(2\omega t) \right] \right) \qquad (5)$$

This force, which is proportional to the electrically induced oscillations of the cantilever during KPFM, is minimized when the applied DC voltage is equal to the surface potential of the sample. The lock-in amplifier of the KPFM system is used to track the cantilever oscillations at ω. This makes the last term of the equation have a negligible effect on the force. The KPFM system is then able to map the surface potential of the sample by applying a DC bias to nullify the oscillations of the cantilever thereby minimizing the capacitive force.

KPFM requires use of an electrically conductive tip. The surface potential that is mapped by KPFM is also the contact potential difference. This is a measure which relies of the WF difference between the tip and the sample. As such, KFPM yeilds a relative work function measurement of the sample with respect to the tip. If the tip work function is calibrated before-hand on a sample with known work function such as highly oriented pyrolytic graphite or gold, then the absolute work function of the sample can be determined using equation 6, where V_{CPD} is the contact potential difference, ϕ_{tip} is the tip WF, ϕ_{sample} is the sample WF, and e is the elementary charge[49].

$$V_{CPD} = \frac{\phi_{tip} - \phi_{sample}}{e}$$

2.6 LITERATURE REVIEW

To date, there have not been investigations directly on the charge screening behaviors of 2D HOIPs. However there have been various studies on the charge screening properties of other 2D materials. These studies used either electrostatic force microscopy (EFM) or KPFM to

investigate the thickness dependent charge screening properties of 2D materials on their own or in heterostructures.

Gomez et al. investigated the charge screening behaviors of MoS_2 layers[50]. In this work they investigated the charge screening behaviors of MoS_2 layers via EFM. They found that the monolayer MoS_2 was ineffective at screening perturbations at the MoS_2-SiO_2 interface, however the screening effect saturates at 20 layers. They also discuss the importance of interlayer coupling effects on the charge screening behavior of MoS_2. Feng et al. also investigated the charge screening behavior of MoS_2 under various humidifies and determined a screening length of 5 layers using KPFM[51]. Similarly, Datta et al. conducted EFM investigations on graphene and determined a charge screening length of five layers[52]. A similar investigation was done using KPFM on graphene by Lee et al. In this study, it was found that the surface potential of graphene decreases exponentially as a function of graphene layers[53]. Additionally, the absolute work function of different layer numbers of graphene were calculated from the KPFM information. A similar study was conducted by Li et al. on hexagonal boron nitride flakes in which it was determined via EFM that h-BN displays weak layer dependency on charge screening[54].

There have also been several studies on heterostructures of the charge screening behaviors of 2D materials. The effect of mixing layers of materials with different electrical properties on screening behaviors of fabricated devices were previously uninvestigated. Li et al. investigated the charge screening behaviors of MoS_2 and graphene heterostructures[55]. They found that their fabricated heterostructures displayed asymmetric electric field screening. They also found that the screening effect could be enhanced by using more MoS_2 layers instead of the graphene layers. These types of heterostructure investigations yields insights into tuning devices based on the material screening properties.

Although much work focused on the layer dependent charge screening nature of HOIPs has not been conducted, there has been some work on HOIP charge screening. For example, Su et al. reported a dielectric-screening effect in formamidinium-cesium lead halide perovskites in solar cell applications[56]. They found that by doping the perovskite with potassium based species they could effectively tune the dielectric response of the perovskite material. These changes lead to changes in the coulomb interactions which in turn affect the defect capture cross section. The defect capture cross section is the probability with which mobile carriers are trapped by defects. By decreasing the defect capture cross sections, the non-radiative recombination pathways are suppressed which leads to a higher performance. The group showed that a solar cell made by tuning the defect screening showed an improved PCE of 22%.

Electrical doping of HOIPs also has an effect on perovskite devices. Electron and hole conductivities depend on the carrier concentration and the carrier mobility. The dependence of carrier mobility on different scattering mechanisms is approximated as the sum contributions of carrier mobility limitations by impurities, phonons, and defects[57]. Introducing dopants into the perovskite matrix contributes to the coulombic interactions and affects the charge mobility of carriers in the materials[5]. Additionally, surface charge doping from contacting interfaces have been shown to shift the work function of the perovskite by charge injection at contact interfaces[58].

3. MATERIALS AND METHODS

3.1 MATERIALS

To investigate how the charge screening behavior depends on the quantum well number, the perovskite samples were standardized with respect to the organic ligand. The perovskite materials used in this study were C4n1, C4n2, C4n3, and C4n5. C4n2 was synthesized by Doyun Kim in the materials science and engineering department at Texas A&M University. The

perovskite flakes were characterized via X-ray diffraction to determine phase purity. C4n1, C4n3, and C4n5 were synthesized by Dr. Ioannis Spanopoulos of Northwestern University. The crystallographic structure of these materials are shown in figure 8 where the pink layers depict the BX_6^- octahedra. These quantum well layers are separated by butyl ammonium ligands which are depicted in grey in the figure.
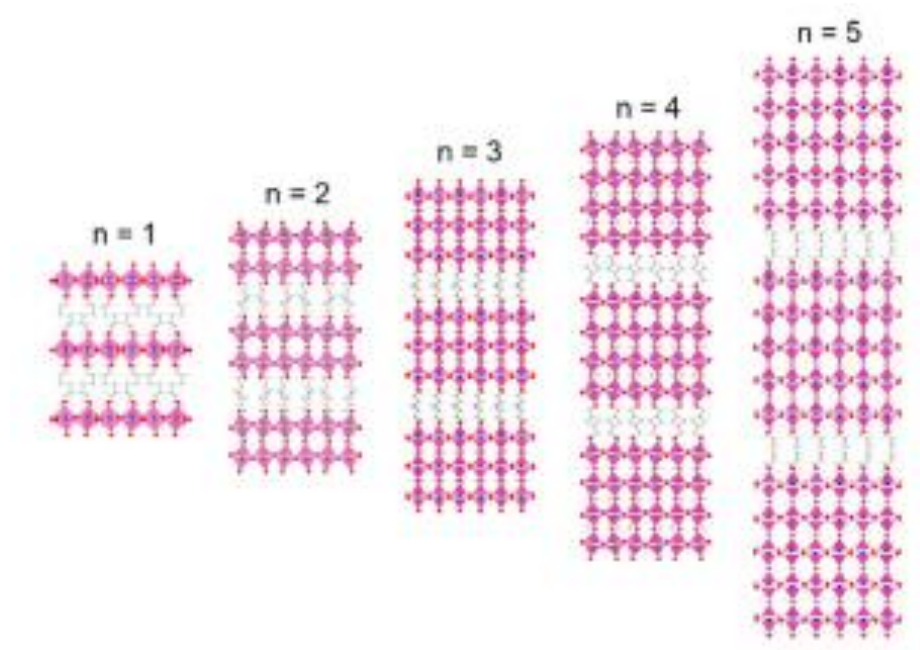
Figure 8: Crystal structures of $(BA)_2(MA)_{n-1}PbI_{3n-1}$ (n= 1, 2, 3, and 5)[59].

Perovskite synthesis follows a general procedure in which PbO precursor is dissolved in HI solution and heated with stirring to form a yellow solution. For n>1 HOIP samples, methylamine hydrochloride is added to this hot solution. In a separate vial, a solution of butyl ammonium in aqueous H_4PO_2 is mixed. The butylammonium solution is then mixed with the PbO dropwise under continuous heating. The solution is thoroughly mixed and then allowed to cool down slowly to room temperature. As the solution cools down, 2D HOIP crystals crash out of

19

solution. These flakes are then filtered out of the solution via suction filtration and dried in a low pressure environment. The flakes are then analyzed for phase purity using XRD. The collected XRD spectrum compared to the calculated spectrum for C4n2 samples used in this experiment are shown in figure 9 as an example. Different HOIPs are synthesized using different precursor ratios. In general, higher n number HOIPs use a larger amount of PbO.
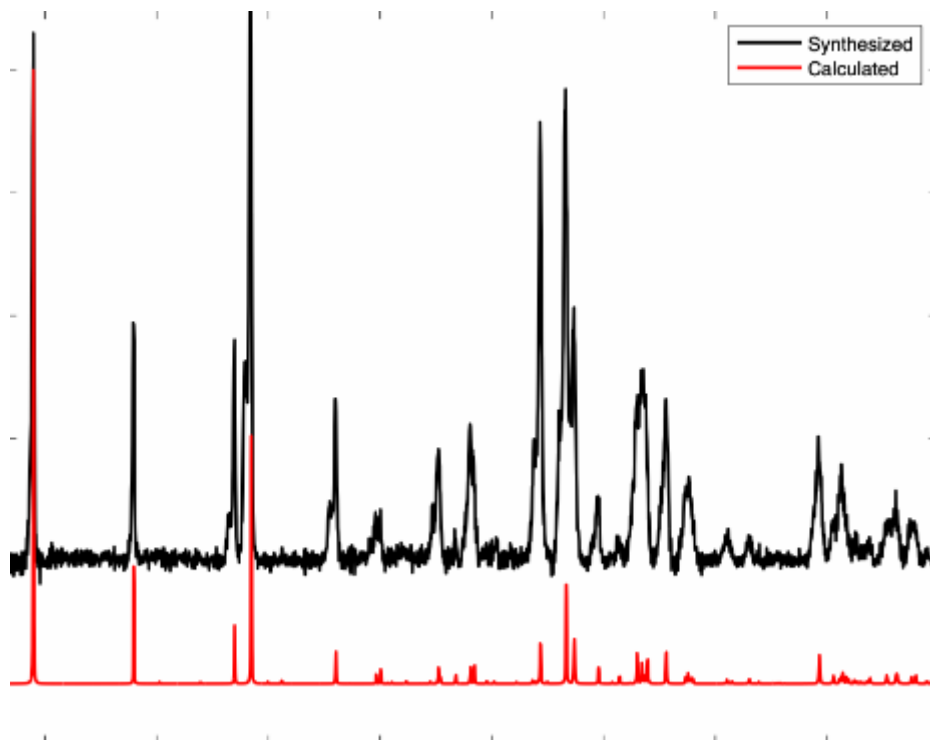
Figure 9: X-ray diffraction spectrum of the synthesized C4n2 flakes used in this research compared to the calculated spectrum.

3.2 SAMPLE PREPARATION

Samples were prepared by mechanical exfoliating perovskite flakes onto clean SiO_2 substrates which were mounted onto a glass slide for analysis under the AFM. First, the SiO_2

substrates were cleaned by ethanol sonication for five minutes and subsequent rinsing with deionized (DI) water. The substrates were then submerged for 20 minutes in a piranha solution which was made my mixing a 3:1 ratio of concentrated sulfuric acid and 30% hydrogen peroxide. During piranha cleaning, the substrates were placed on a glass vial on top of a hot plate which was heated to 115°C.

When dealing with perovskite samples, much care was taken to reduce exposure of the flakes to the ambient environment. This was a precautionary measure taken to ensure that the perovskite samples would not degrade in the presence of ambient humidity. The ambient humidity in the lab was measured with a hygrometer and noted to be between 40-60% RH. A glove box was used during sample preparation, specifically mechanical exfoliation, of the perovskite samples. The humidity within the glove box was controlled by introducing a constant flow of dry air. The relative humidity within the glove box generally fluctuated between 3-10% RH. Furthermore, the AFM was modified by sealing the AFM head with a plastic bag with was taped down to ensure a good seal. A dry air line was also introduced to this set up to maintain a humidity of 3-4% RH in the AFM head when the system stabilized.

After piranha cleaning, the substate was rinsed well with DI water and then dried by blowing dry air over the substrate. Substrate was handled with cleaned tweezers. The substrate and perovskite sample of interest was then placed inside the glove box which had stabilized to a dry environment. Perovskite crystals were then mechanically exfoliated 8 times using scotch tape to create a grid of samples and transferred to the substrate surface. The now exfoliated perovskite sample on the substrate was then mounted on a glass slide using scotch tape. A grounding wire was attached to the glass slide and electrically connected to the substrate surface using electrically

conductive silver paste to ground the sample. The sample was then transferred to the AFM in a petri dish with desiccant to further limit the effects of humidity on the sample.

3.3 EXPERIMENTAL PROCEDURE

AFM and KPFM images were taken using an Asylum Research MFP 3D Infinity. A conductive cantilever was chosen for KPFM measurements but was also used for topographic imaging. The cantilevers used were Budget Sensor ElectriMulti75-G. These cantilevers have a typical force constant of 3 N/m, with a resonance frequency in the 60-90 kHz range and a tip radius of less than 25 nm. These cantilevers have a conductive chromium and platinum coating. The cantilever was mounted and tuned for tapping mode.

While on the AFM stage under a dry environment (4% RH), thin to thick flakes of each perovskite were identified and KFPM images of the flakes were taken. Good sample areas consisted of monolayer, bilayer, and thicker flakes up to bulk samples. These areas were first identified via optical contrast on the AFM camera based on the flake color and transparency. These areas were then confirmed to be good sample areas by conducting topography imaging. Topographic height of the flakes were used to determine the layer number. Once a good sample area was found, electrical tuning for KPFM was done and the KPFM scan was conducted at a very slow (0.25 Hz) scan rate. This scan rate was necessary to avoid tip contamination which would change the measured contact potential difference by the KPFM.

Acquired images were then analyzed by drawing masks using the AFM software on the images to obtain histograms of surface potential data from masked areas. The histograms of the surface potential data was then fit using a gaussian fit to determine the standard deviation and mean contact potential difference for each layer thickness for all of the 2D HOIPs analyzed.

4. RESULTS AND DISCUSSION

4.1 C4n1

C4n1 perovskites displayed a relatively weaker charge screening behavior compared to the higher n number 2D HOIPs. As seen in figure 10, the perovskite effectively screens charge perturbations at a thickness of about 18 nm where the normalized contact potential difference is shown to plateau. The monolayer of C4n1 seen at the bottom of figure 10 clearly shows a contrast from the adjacent slightly thicker flake of about 5 nm and the bulk flake which is about 40 nm thick. In this image, there is a slight gap in the data after 20 nm which makes it unclear if the contact potential difference truly plateaus, however it was confirmed that the surface potentials of C4n1 at and greater than 20 nm do not show a significant difference in another round of imaging.
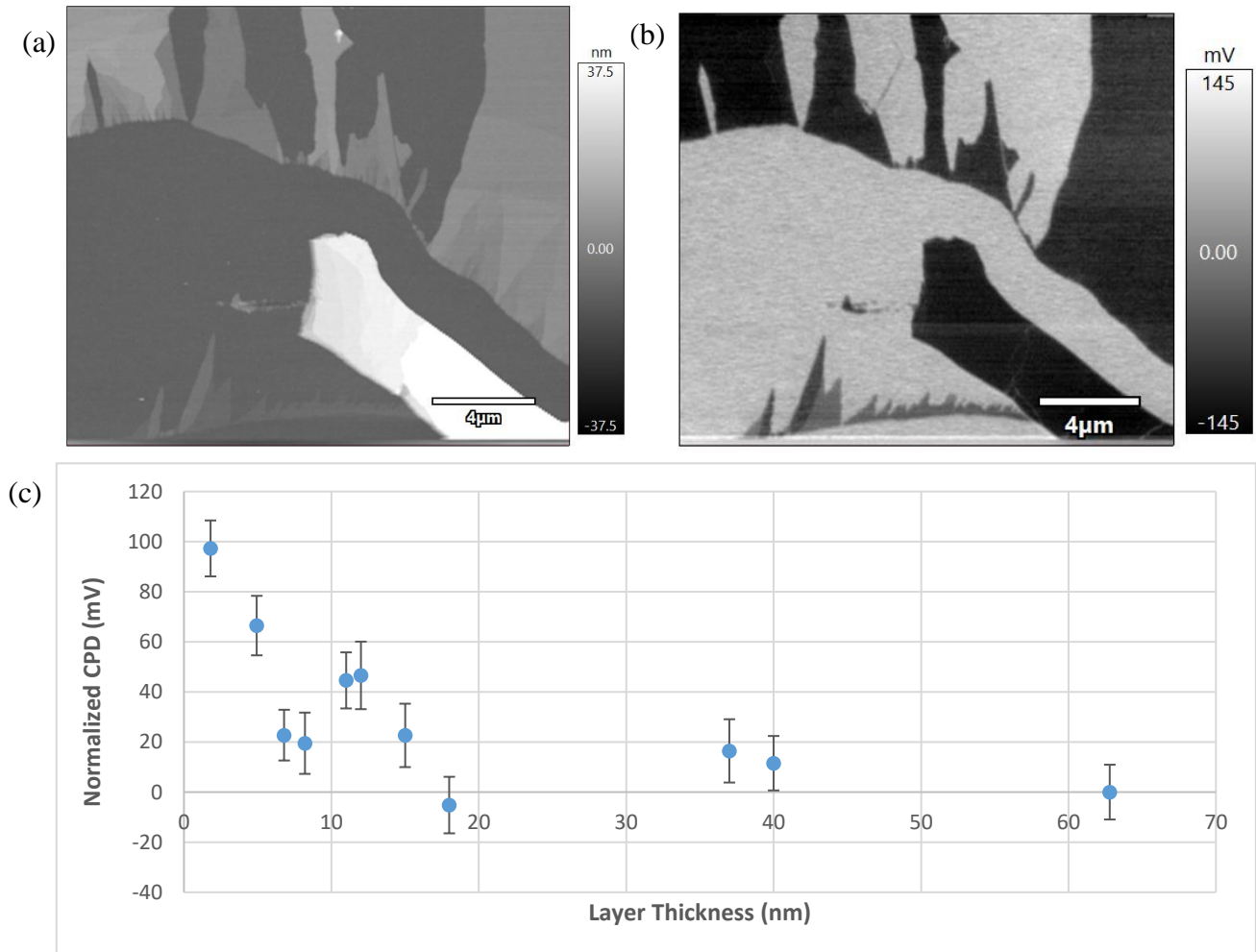
Figure 10: Topography, surface potential and normalized contact potential difference graph of C4n1.

4.2 C4n2

C4n2 displays a slightly stronger charge screening behavior compared to C4n1. C4n2 seems to completely screen out charge perturbations at a thickness of about 11 nm. Figure 11 shows monolayer up to bulkier surface potentials of C4n2, however this data on its own is ambiguous and unclear as to the charge screening length of this material. Figure 12 shows another set of thicker flakes that were scanned to determine the true plateau point of this material. This set of data convincingly shows that the surface potential does not significantly change after 11 nm.

(a)

(b)

(c)
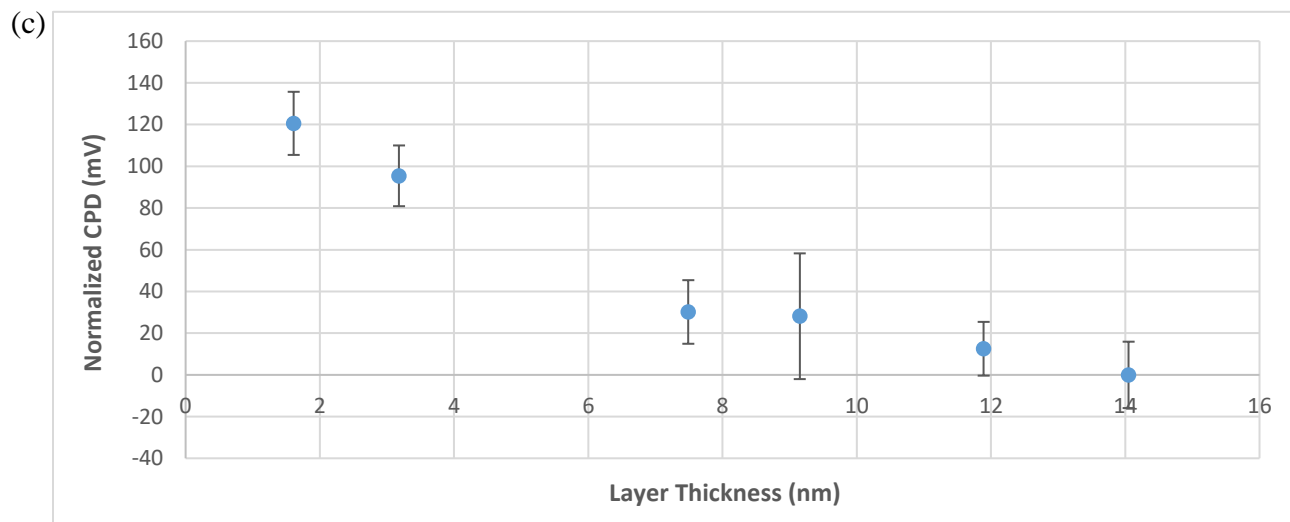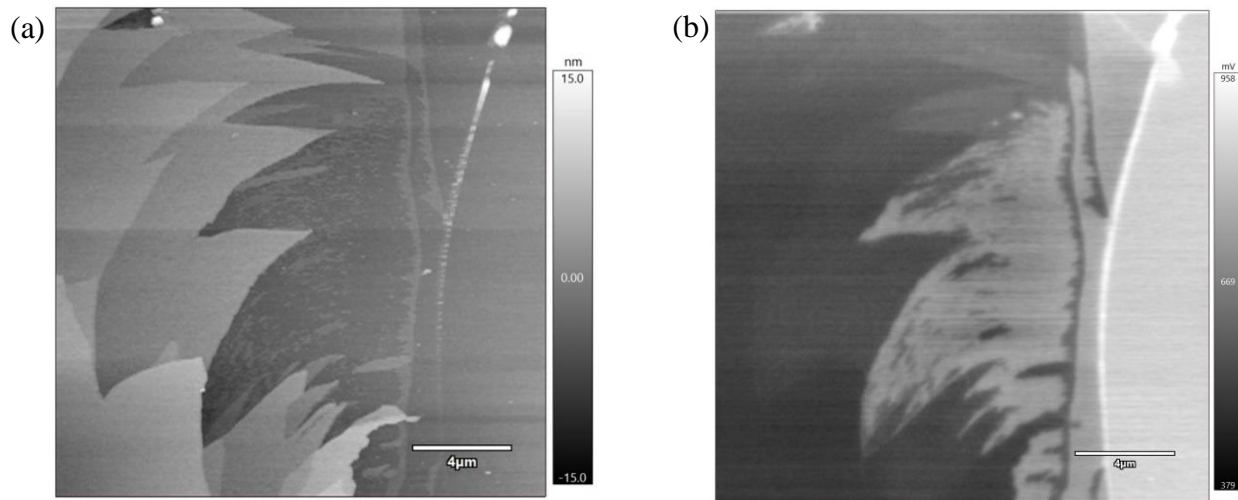
Figure 11: Topography, surface potential and normalized contact potential difference graph of C4n2.

(a)

(b)

(c)
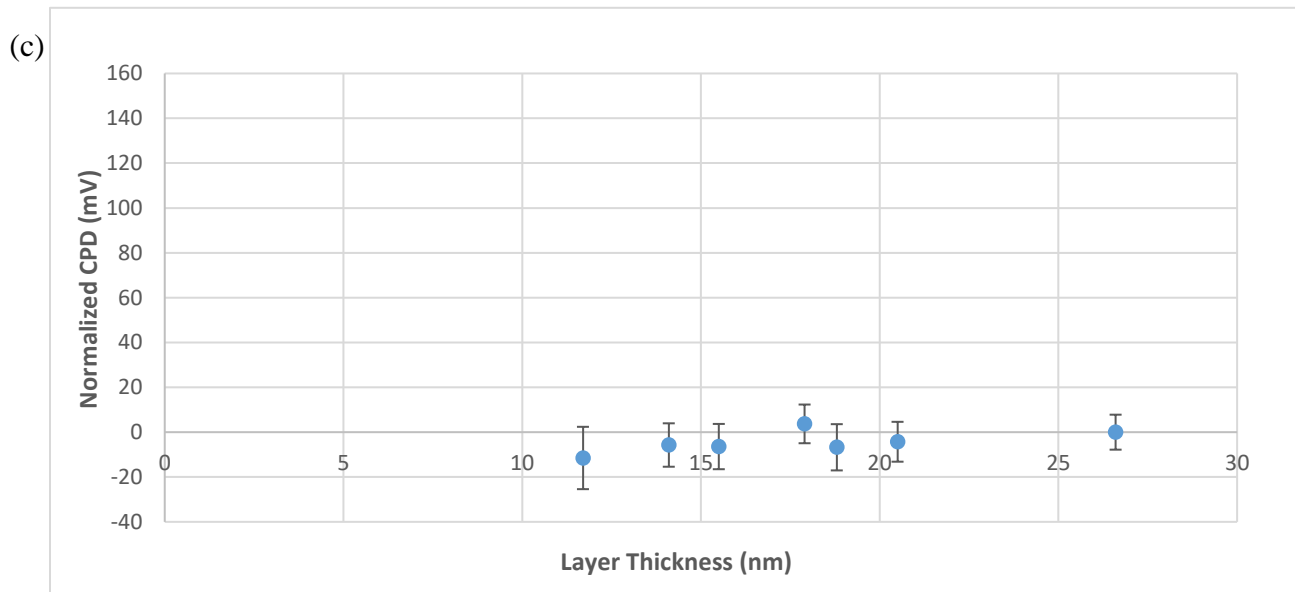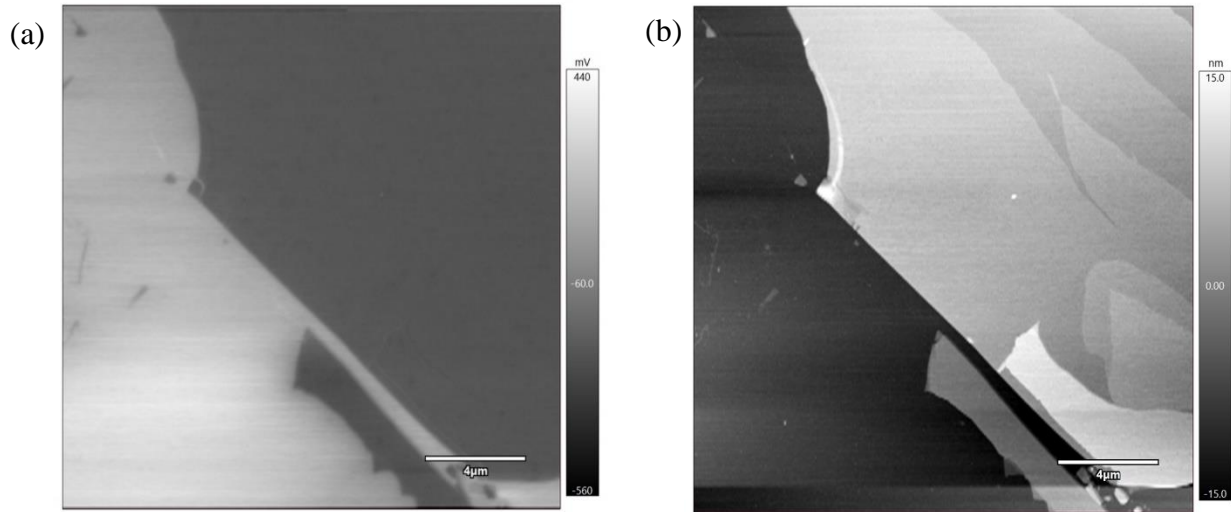
Figure 12: Topography, surface potential and normalized contact potential difference graph of thicker C4n2 flakes to determine the screening length.

4.3 C4n3

C4n3 shows stronger charge screening behavior as the surface potential of this sample plateaus quicker with layer number compared to the C4n1 and C4n2 flakes. Charge perturbations

are completely screened by this material with close to just four layers of material, corresponding to a thickness of about 10 nm as seen in figure 13c.

(a)

(b)

(c)

Figure 13: Topography, surface potential and normalized contact potential difference graph of C4n3

This data set contains a large gap between 15 and 25 nm which was filled by collecting some data from thicker flakes which is shown in figure 14a. The trend from this data set and the previous data set are in good agreement with each other however additional data filling the gap between 15 and 20 nm is needed.

(a)

(b)

(c)

Figure 14: Topography, surface potential and normalized contact potential difference graph of thicker C4n3 flakes to determine the screening length.

(a)

(b)

(c)
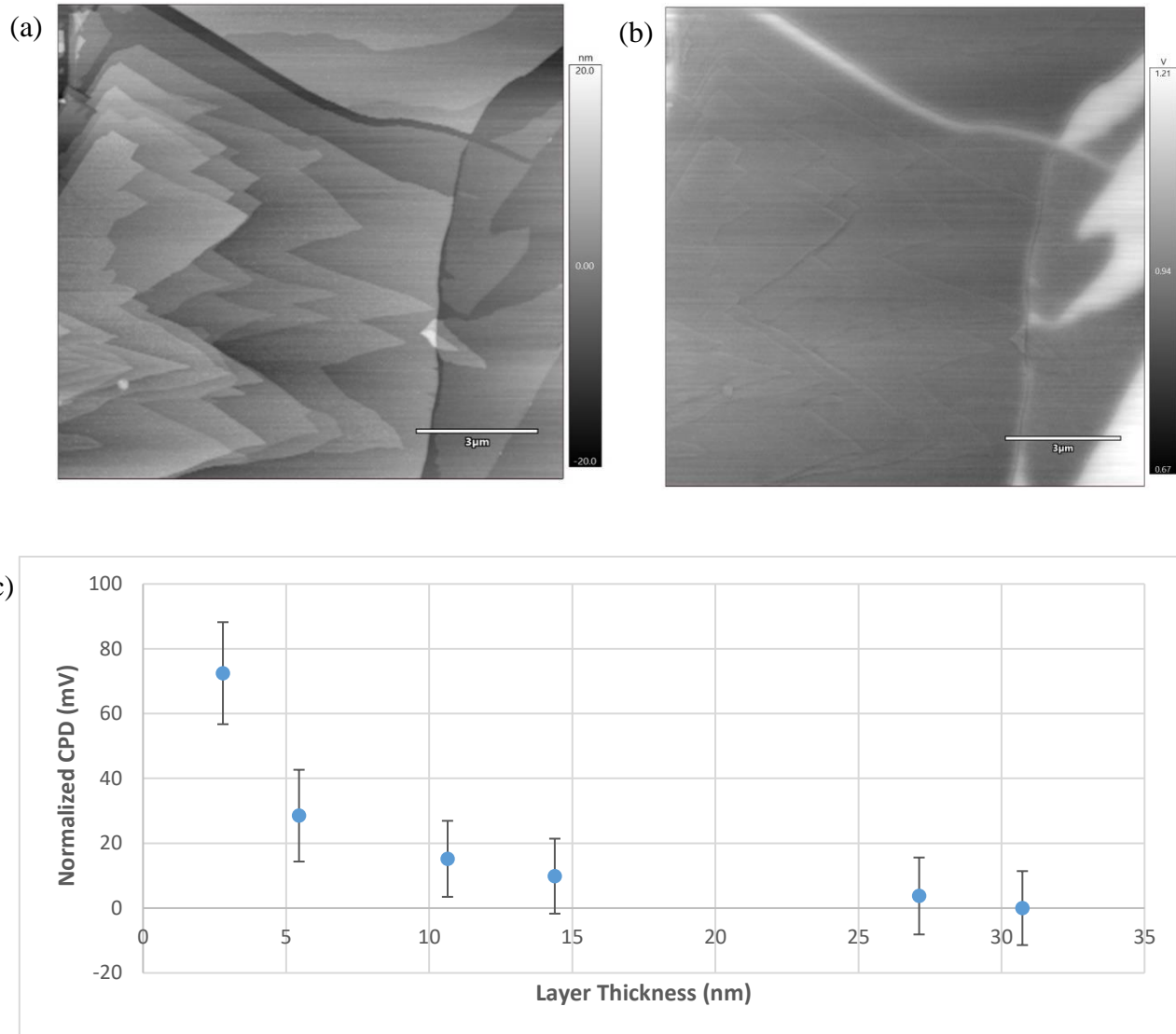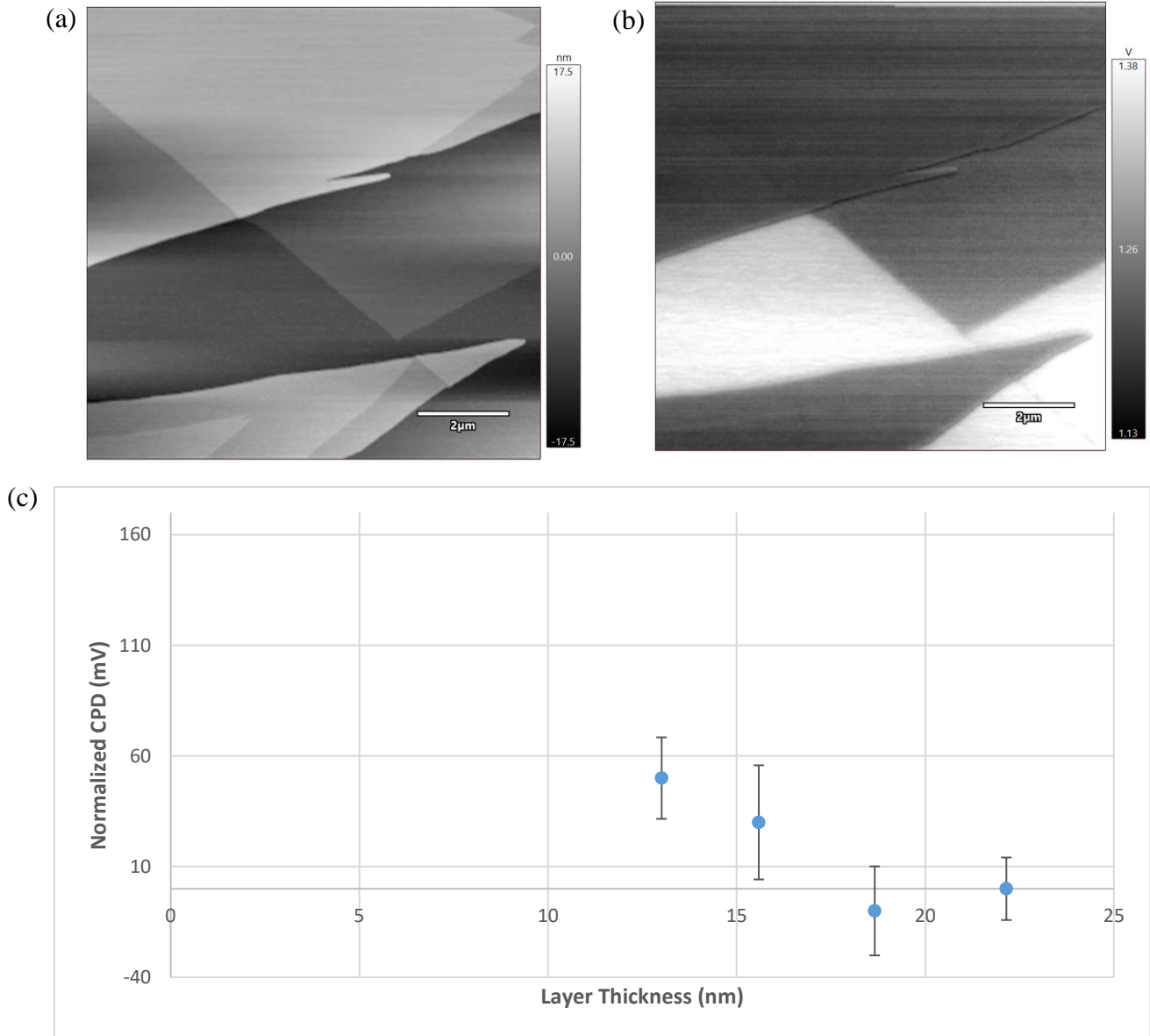

Figure 15: Topography, surface potential and normalized contact potential difference graph of thicker C4n3 flakes to determine the screening length with data between 15 and 20 nm.
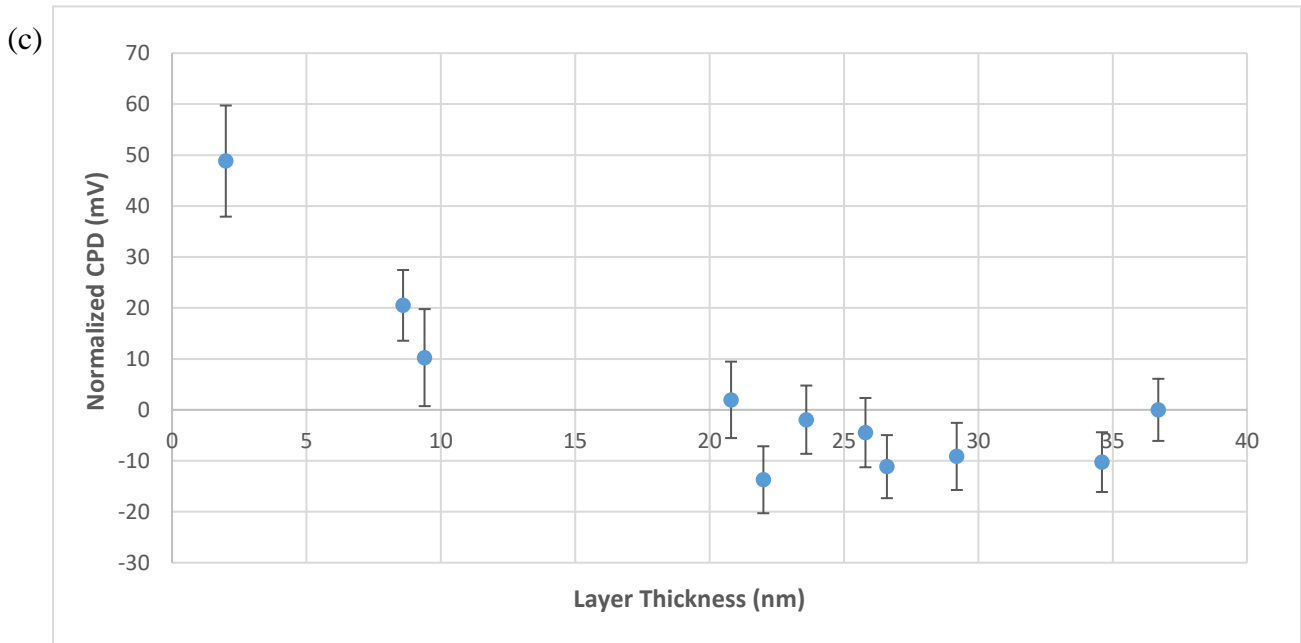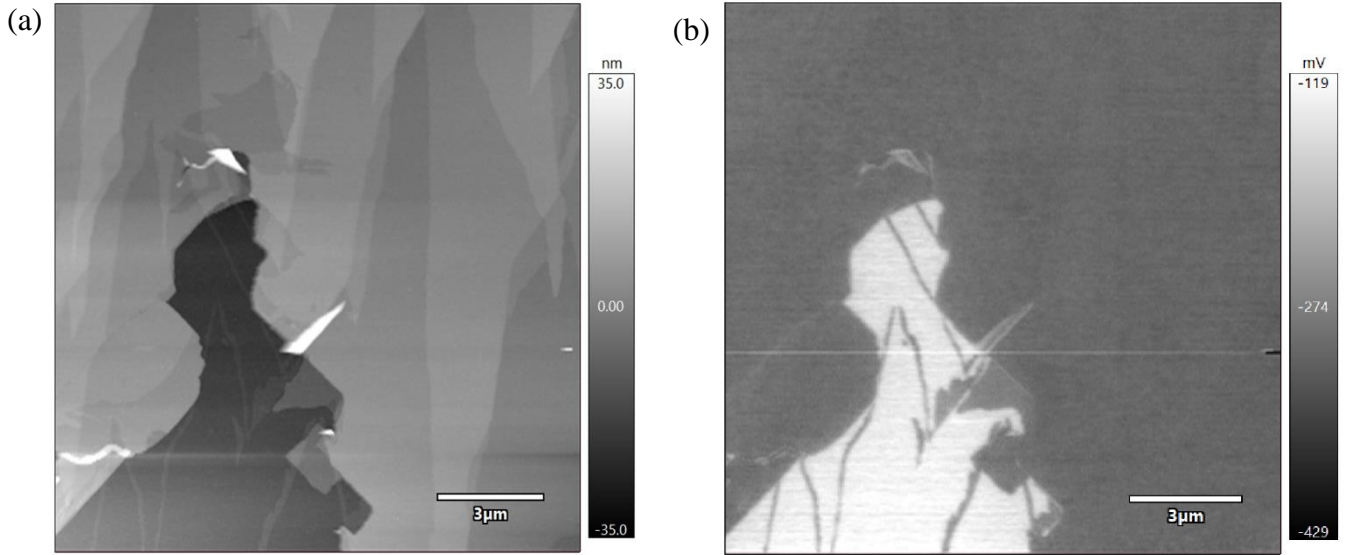
Figure 15c shows the data filling the gap between 15 and 20 nm and shows that the charge screening length is about 15 nm for c4n3.

4.4 C4n5

C4n5 shows the strongest charge screening behavior by far. After just a monolayer of this materials charge perturbations are completely screened out. This can be seen in figure 16b which shows the monolayer with clear contrast in the contact potential difference compared to the adjacent bilayer, trilayer, four-layer flake and five-layer flake.

(a)

(b)

(c)
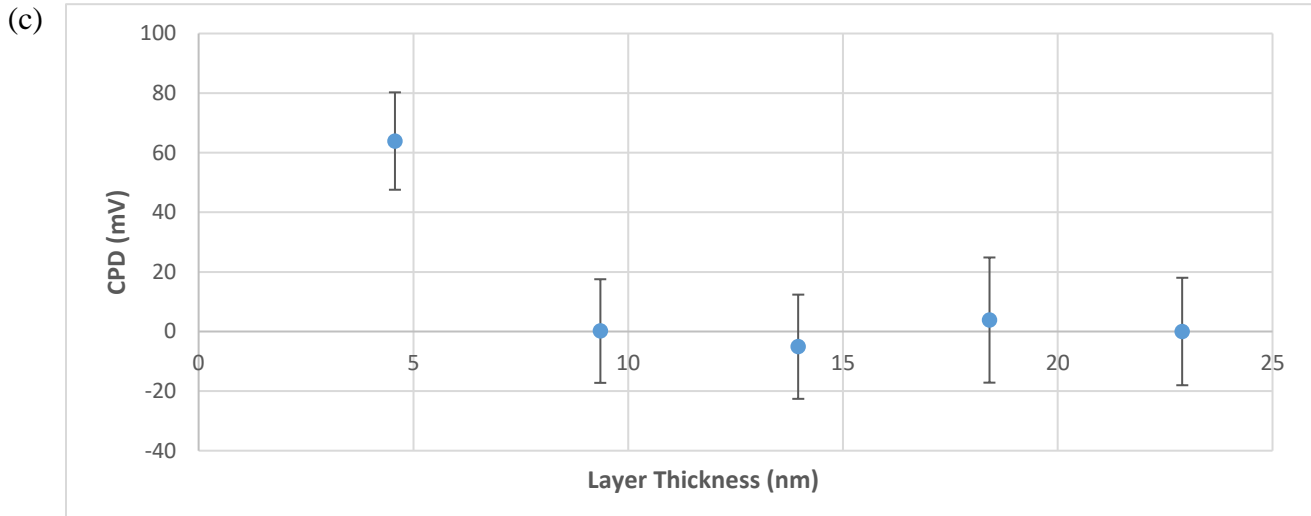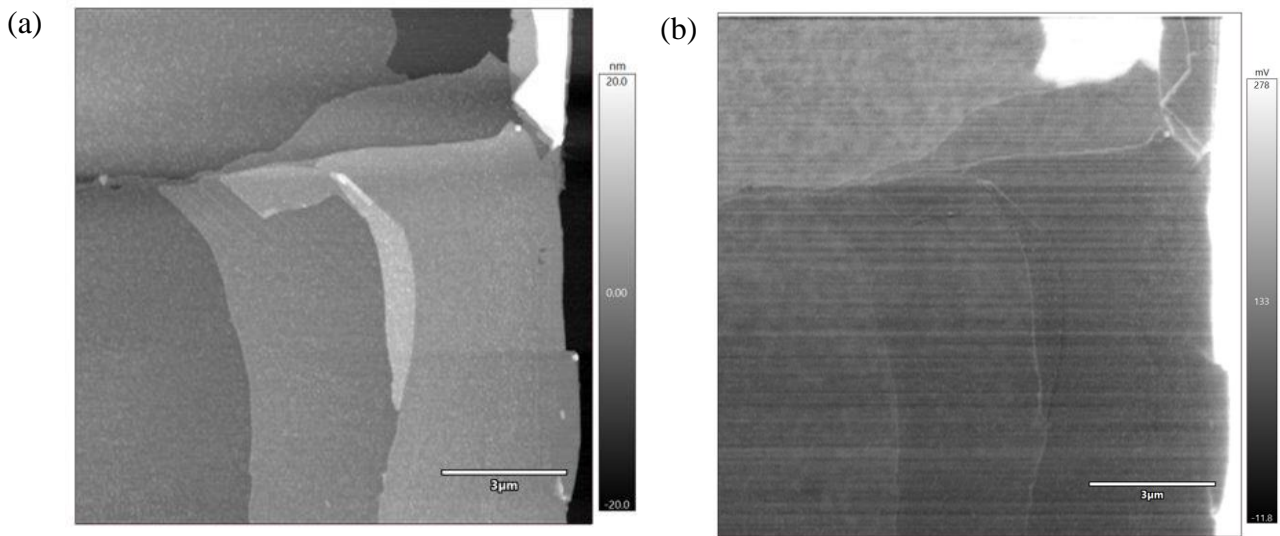
Figure 16: Topography, surface potential and normalized contact potential difference graph of C4n5.

From these results, we learn the dependence of 2D perovskite charge screening on the quantum well number. As the quantum well number increases, the charge screening effect becomes stronger. These results may inspire studies which investigate the physical role of the inorganic layer on increasing the charge screening effect. Furthermore, we see a very strong charge screening effect from C4n5. The surface potential plateaus at a bilayer which is about 7 nm thick which is the charge screening length of C4n5. We can compare this charge screening effect to other 2D materials such as graphene, MoS_2, and hexagonal boronitride (BN) which was investigated using similar methodology[50, 52-54]. In these experiments, the charge screening length of 5 graphene layers is extrapolated from the data which corresponds to approximately 1.7 nm thick. The charge screening length of MoS_2 was determined to be approximately 7 nm. The charge screening length of BN was found to be much larger at approximately 80 nm.

Compared to these 2D materials, the 2D perovskites measured in this study display tunable charge screening lengths between that of MoS_2 and Graphene. The charges screening effect of these materials is stronger than that compared to BN which displays a very weak thickness dependent charge screening behavior.

Charge screening behavior is dependent on the substrate-semiconductor interaction. The charge screening length of materials can be thought of as the length at which charge exchange from the substrate ceases to influence the charge distribution in the semiconducting material. 2-Dimensional materials have layered structures in which weak Van Der Waals interactions hold the layers together. As such the out-of-plane charge carrier properties of 2D may influence the charge screening lengths.

From this we might gather that the organic dielectric layer of the perovskite materials may play a crucial role in their charge screening behavior. Additionally, the physical distance for out-of-plane charge transfer for 2D perovskite monolayers increases with increasing n number. These two factors may explain the trend in increasing the quantum well number as well as the sharp thickness dependent charge screening behavior of C4n5.

One other contributor to the screening behavior is the interstitial A site cations in the 2D perovskite materials. In this experiment these cations are methylammonium (MA) cations. Layers of these interstitial organic cations are found between the octahedra of the inorganic layers as shown pictured in figure 4. It is also important to note that the A site cations are not present in C4n1 as there are no interstitial areas for them to be as there is only one layer of inorganic octahedra. A previous study on 3D HOIP thin films with blended MA and FA A site cations investigated the influence of the A site cation on the charge transport properties, including screening, of the film[60]. In this study, it was found that for 0% and 75% FA HOIPs involved fast charge screening mechanisms based on electronic and ionic coupling mechanisms Whereas redistribution compared to fast charge transport processes in the 15% FA HOIP. This study outlined the importance of ionic conduction mechanisms and how the A site cations may affect this conduction mechanism. The trend seen in this study may also be related to the different amount of MA A site cations present in the different 2D HOIPs samples leading to different screening behaviors.

Additionally, these results speak to the tunability of 2D HOIPs. The result of this study guides the engineering of devices based on the application needs. The perovskite materials may be synthesized with specific quantum well thicknesses to accommodate application needs now that this dependence is known.

5. CONCLUSIONS AND FUTURE WORK

5.1 SUMMARY

In conclusion, this study elucidates the charge screening behavior of 2D RP HOIPs and the dependence of the charge screening length on the quantum well number. The results show a trend of higher n number perovskites having a stronger charge screening effect. This is indicated by a decreased charge screening length of the HOIP samples as the n number increases. C4n1 shows the weakest charge screening behavior, in stark contrast C4n5 displays very strong charge screening behavior as a bilayer is enough to completely screen all charge perturbations. This study opens the path to informing the engineering of efficient semiconducting devices based on 2D perovskite materials which are unhindered by charge perturbations.

Table 1: Summary of charge screening lengths of 2D perovskite samples

Sample	Charge Screening Length (nm)
C4n1	18
C4n2	12
C4n3	10
C4n5	7

5.2 FUTURE WORK

This study only looked at some samples from the butylammonium family of 2D perovskites. 2D perovskites are very versatile and highly tunable materials because the ease with which their structures can be manipulated. Many 2D perovskites have been synthesized using longer chain alkylammonium ligands[61]. A similar study to this one can be conducted to determine the effect of elongating the organic ligand on the charge screening behavior. The organic ligands discussed until this point have been linear alkyl ammonium chains. However, 2D perovskites with aromatic phenyl ammonium ligands have also been synthesized and investigated[62]. This study can also be expanded to studying the charge screening behavior of these materials.

A natural next step from this study is to implement the different perovskite materials in small scale devices and measuring their performance. This type of study will serve to confirm that these materials can be used at their respective charge screening lengths to improve the efficiency of these devices without sacrificing size. This can be done by comparing the performance of devices made with 2D HOIPs below their charge screening length and above it.

REFERENCES

1. Lee, M. M.; Teuscher, J.; Miyasaka, T.; Murakami, T. N.; Snaith, H. J., Efficient hybrid solar cells based on meso-superstructured organometal halide perovskites. *Science* **2012,** *338* (6107), 643-647.

2. Xing, G.; Mathews, N.; Lim, S. S.; Yantara, N.; Liu, X.; Sabba, D.; Grätzel, M.; Mhaisalkar, S.; Sum, T. C., Low-temperature solution-processed wavelength-tunable perovskites for lasing. *Nature Materials* **2014,** *13* (5), 476-480.

3. Oga, H.; Saeki, A.; Ogomi, Y.; Hayase, S.; Seki, S., Improved Understanding of the Electronic and Energetic Landscapes of Perovskite Solar Cells: High Local Charge Carrier Mobility, Reduced Recombination, and Extremely Shallow Traps. *Journal of the American Chemical Society* **2014,** *136* (39), 13818-13825.

4. Wehrenfennig, C.; Eperon, G. E.; Johnston, M. B.; Snaith, H. J.; Herz, L. M., High Charge Carrier Mobilities and Lifetimes in Organolead Trihalide Perovskites. *Advanced Materials* **2014,** *26* (10), 1584-1589.

5. Euvrard, J.; Yan, Y.; Mitzi, D. B., Electrical doping in halide perovskites. *Nature Reviews Materials* **2021,** *6* (6), 531-549.

6. Saparov, B.; Mitzi, D. B., Organic–Inorganic Perovskites: Structural Versatility for Functional Materials Design. *Chemical Reviews* **2016,** *116* (7), 4558-4596.

7. Snaith, H. J., Present status and future prospects of perovskite photovoltaics. *Nature Materials* **2018,** *17* (5), 372-376.

8. Lu, M.; Zhang, Y.; Wang, S.; Guo, J.; Yu, W. W.; Rogach, A. L., Metal Halide Perovskite Light-Emitting Devices: Promising Technology for Next-Generation Displays. *Advanced Functional Materials* **2019,** *29* (30), 1902008.

9.   Yang, T.; Wu, Q.; Dai, F.; Huang, K.; Xu, H.; Liu, C.; Chen, C.; Hu, S.; Liang, X.; Liu, X.; Noh, Y.-Y.; Liu, C., Understanding, Optimizing, and Utilizing Nonideal Transistors Based on Organic or Organic Hybrid Semiconductors. *Advanced Functional Materials* **2020,** *30* (20), 1903889.

10.   Stylianakis, M. M.; Maksudov, T.; Panagiotopoulos, A.; Kakavelakis, G.; Petridis, K. Inorganic and Hybrid Perovskite Based Laser Devices: A Review *Materials (Basel)* [Online], 2019. PubMed. http://europepmc.org/abstract/MED/30875786

https://doi.org/10.3390/ma12060859

https://europepmc.org/articles/PMC6470628

https://europepmc.org/articles/PMC6470628?pdf=render (accessed 2019/03//).

11.   Xie, C.; Liu, C.-K.; Loi, H.-L.; Yan, F., Perovskite-Based Phototransistors and Hybrid Photodetectors. *Advanced Functional Materials* **2020,** *30* (20), 1903907.

12.   (NREL), N. R. E. L. Best Research-Cell Efficiency Chart. https://www.nrel.gov/pv/cell-efficiency.html.

13.   Luo, D.; Su, R.; Zhang, W.; Gong, Q.; Zhu, R., Minimizing non-radiative recombination losses in perovskite solar cells. *Nature Reviews Materials* **2020,** *5* (1), 44-60.

14.   Zhang, Y.; Brar, V. W.; Girit, C.; Zettl, A.; Crommie, M. F., Origin of spatial charge inhomogeneity in graphene. *Nature Physics* **2009,** *5* (10), 722-726.

15.   Callister, W. D.; Rethwisch, D. G., *Materials science and engineering : an introduction*. 2010.

16.   Jastrzebski, Z. D., *Nature and properties of engineering materials*. John Wiley and Sons, Inc.,New York: United States, 1976.

17.   Kahn, A., Fermi level, work function and vacuum level. *Materials Horizons* **2016,** *3* (1), 7-10.

18.   Wells, A. F., *Structural inorganic chemistry*. Oxford university press: 2012.

19.   Weller, M. T.; Weber, O. J.; Henry, P. F.; Di Pumpo, A. M.; Hansen, T. C., Complete structure and cation orientation in the perovskite photovoltaic methylammonium lead iodide between 100 and 352 K. *Chemical communications* **2015,** *51* (20), 4180-4183.

20.   Stoumpos, C. C.; Malliakas, C. D.; Kanatzidis, M. G., Semiconducting tin and lead iodide perovskites with organic cations: phase transitions, high mobilities, and near-infrared photoluminescent properties. *Inorganic chemistry* **2013,** *52* (15), 9019-9038.

21.   Goldschmidt, V. M., Die gesetze der krystallochemie. *Naturwissenschaften* **1926,** *14* (21), 477-485.

22.   Travis, W.; Glover, E. N. K.; Bronstein, H.; Scanlon, D. O.; Palgrave, R. G., On the application of the tolerance factor to inorganic and hybrid halide perovskites: a revised system. *Chemical Science* **2016,** *7* (7), 4548-4556.

23.   Chen, X.; Zhou, H.; Wang, H., 2D/3D Halide Perovskites for Optoelectronic Devices. *Frontiers in Chemistry* **2021,** *9* (679).

24.   Wang, Z.; Shi, Z.; Li, T.; Chen, Y.; Huang, W., Stability of Perovskite Solar Cells: A Prospective on the Substitution of the A Cation and X Anion. *Angewandte Chemie (International ed. in English)* **2017,** *56* (5), 1190-1212.

25.   Burschka, J.; Pellet, N.; Moon, S.-J.; Humphry-Baker, R.; Gao, P.; Nazeeruddin, M. K.; Grätzel, M., Sequential deposition as a route to high-performance perovskite-sensitized solar cells. *Nature* **2013,** *499* (7458), 316-319.

26.   Leguy, A. M. A.; Hu, Y.; Campoy-Quiles, M.; Alonso, M. I.; Weber, O. J.; Azarhoosh, P.; van Schilfgaarde, M.; Weller, M. T.; Bein, T.; Nelson, J.; Docampo, P.; Barnes, P. R. F., Reversible Hydration of CH3NH3PbI3 in Films, Single Crystals, and Solar Cells. *Chemistry of Materials* **2015,** *27* (9), 3397-3407.

27. Frost, J. M.; Butler, K. T.; Brivio, F.; Hendon, C. H.; Van Schilfgaarde, M.; Walsh, A., Atomistic origins of high-performance in hybrid halide perovskite solar cells. *Nano letters* **2014,** *14* (5), 2584-2590.

28. Noh, J. H.; Im, S. H.; Heo, J. H.; Mandal, T. N.; Seok, S. I., Chemical management for colorful, efficient, and stable inorganic–organic hybrid nanostructured solar cells. *Nano letters* **2013,** *13* (4), 1764-1769.

29. Lee, M. M.; Teuscher, J.; Miyasaka, T.; Murakami, T. N.; Snaith, H. J., Efficient hybrid solar cells based on meso-superstructured organometal halide perovskites. *Science* **2012,** *338* (6107), 643-647.

30. Yang, J.; Siempelkamp, B. D.; Liu, D.; Kelly, T. L., Investigation of CH3NH3PbI3 degradation rates and mechanisms in controlled humidity environments using in situ techniques. *ACS nano* **2015,** *9* (2), 1955-1963.

31. Christians, J. A.; Miranda Herrera, P. A.; Kamat, P. V., Transformation of the excited state and photovoltaic efficiency of CH3NH3PbI3 perovskite upon controlled exposure to humidified air. *Journal of the American Chemical Society* **2015,** *137* (4), 1530-1538.

32. Agmon, N., The grotthuss mechanism. *Chemical Physics Letters* **1995,** *244* (5-6), 456-462.

33. Sutton, R. J.; Eperon, G. E.; Miranda, L.; Parrott, E. S.; Kamino, B. A.; Patel, J. B.; Hörantner, M. T.; Johnston, M. B.; Haghighirad, A. A.; Moore, D. T., Bandgap-tunable cesium lead halide perovskites with high thermal stability for efficient solar cells. *Advanced Energy Materials* **2016,** *6* (8), 1502458.

34. Kim, H.; Lee, C.; Im, J.; Lee, K.; Moehl, T.; Marchioro, A., & Grätzel, M.(2012). Lead iodide perovskite sensitized all-solid-state submicron thin film mesoscopic solar cell with efficiency exceeding 9%. *Scientific reports 2*, 591.

35.   Chen, Y.; Sun, Y.; Peng, J.; Tang, J.; Zheng, K.; Liang, Z., 2D Ruddlesden–Popper Perovskites for Optoelectronics. *Advanced Materials* **2018,** *30* (2), 1703487.

36.   Tsai, H.; Nie, W.; Blancon, J.-C.; Stoumpos, C. C.; Asadpour, R.; Harutyunyan, B.; Neukirch, A. J.; Verduzco, R.; Crochet, J. J.; Tretiak, S., High-efficiency two-dimensional Ruddlesden–Popper perovskite solar cells. *Nature* **2016,** *536* (7616), 312-316.

37.   Kagan, C. R.; Mitzi, D. B.; Dimitrakopoulos, C. D., Organic-inorganic hybrid materials as semiconducting channels in thin-film field-effect transistors. *Science* **1999,** *286* (5441), 945-947.

38.   Cao, D. H.; Stoumpos, C. C.; Farha, O. K.; Hupp, J. T.; Kanatzidis, M. G., 2D homologous perovskites as light-absorbing materials for solar cell applications. *Journal of the American Chemical Society* **2015,** *137* (24), 7843-7850.

39.   Smith, I. C.; Hoke, E. T.; Solis-Ibarra, D.; McGehee, M. D.; Karunadasa, H. I., A layered hybrid perovskite solar-cell absorber with enhanced moisture stability. *Angewandte Chemie International Edition* **2014,** *53* (42), 11232-11235.

40.   Ansari, M. I. H.; Qurashi, A.; Nazeeruddin, M. K., Frontiers, opportunities, and challenges in perovskite solar cells: A critical review. *Journal of Photochemistry and Photobiology C: Photochemistry Reviews* **2018,** *35*, 1-24.

41.   Koh, T. M.; Shanmugam, V.; Schlipf, J.; Oesinghaus, L.; Müller-Buschbaum, P.; Ramakrishnan, N.; Swamy, V.; Mathews, N.; Boix, P. P.; Mhaisalkar, S. G., Nanostructuring Mixed-Dimensional Perovskites: A Route Toward Tunable, Efficient Photovoltaics. *Advanced Materials* **2016,** *28* (19), 3653-3661.

42.   Pimenta-Lopes, C.; Suay-Corredera, C.; Velázquez-Carreras, D.; Sánchez-Ortiz, D.; Alegre-Cebollada, J., Concurrent atomic force spectroscopy. *Communications Physics* **2019,** *2* (1), 91.

43.   Alexander, J.; Belikov, S.; Magonov, S., AFM-Based Characterization of Electrical Properties of Materials. In *Nanoscale Imaging: Methods and Protocols*, Lyubchenko, Y. L., Ed. Springer New York: New York, NY, 2018; pp 99-127.

44.   Zhang, Y.; Zhu, W.; Hui, F.; Lanza, M.; Borca-Tasciuc, T.; Muñoz Rojo, M., A Review on Principles and Applications of Scanning Thermal Microscopy (SThM). *Advanced Functional Materials* **2020,** *30* (18), 1900892.

45.   Passeri, D.; Dong, C.; Reggente, M.; Angeloni, L.; Barteri, M.; Scaramuzzo, F. A.; De Angelis, F.; Marinelli, F.; Antonelli, F.; Rinaldi, F.; Marianecci, C.; Carafa, M.; Sorbo, A.; Sordi, D.; Arends, I. W.; Rossi, M., Magnetic force microscopy: quantitative issues in biomaterials. *Biomatter* **2014,** *4*, e29507.

46.   Dufrêne, Y. F.; Ando, T.; Garcia, R.; Alsteens, D.; Martinez-Martin, D.; Engel, A.; Gerber, C.; Müller, D. J., Imaging modes of atomic force microscopy for application in molecular and cell biology. *Nature nanotechnology* **2017,** *12* (4), 295-307.

47.   Veerapandian, M.; Yun, K., Study of Atomic Force Microscopy in Pharmaceutical and Biopharmaceutical Interactions - A Mini Review. *Current Pharmaceutical Analysis* **2009,** *5*, 256-268.

48.   Research, A., Applications Guide. *SPM Applications Guide* **2018,** *User Guide 3*, 138-139.

49.   Fernández Garrillo, P. A.; Grévin, B.; Chevalier, N.; Borowik, Ł., Calibrated work function mapping by Kelvin probe force microscopy. *Review of Scientific Instruments* **2018,** *89* (4), 043702.

50.   Castellanos-Gomez, A.; Cappelluti, E.; Roldán, R.; Agraït, N.; Guinea, F.; Rubio-Bollinger, G., Electric-Field Screening in Atomically Thin Layers of MoS2: the Role of Interlayer Coupling. *Advanced Materials* **2013,** *25* (6), 899-903.

51.   Feng, Y.; Zhang, K.; Li, H.; Wang, F.; Zhou, B.; Fang, M.; Wang, W.; Wei, J.; Wong, H. S. P.,

        In situvisualization and detection of surface potential variation of mono and multilayer

        MoS2under different humidities using Kelvin probe force microscopy. *Nanotechnology* **2017,** *28*

        (29), 295705.

52.   Datta, S. S.; Strachan, D. R.; Mele, E. J.; Johnson, A. T. C., Surface Potentials and Layer Charge

        Distributions in Few-Layer Graphene Films. *Nano Letters* **2009,** *9* (1), 7-11.

53.   Lee, N. J.; Yoo, J. W.; Choi, Y. J.; Kang, C. J.; Jeon, D. Y.; Kim, D. C.; Seo, S.; Chung, H. J.,

        The interlayer screening effect of graphene sheets investigated by Kelvin probe force

        microscopy. *Applied Physics Letters* **2009,** *95* (22), 222107.

54.   Li, L. H.; Santos, E. J. G.; Xing, T.; Cappelluti, E.; Roldán, R.; Chen, Y.; Watanabe, K.;

        Taniguchi, T., Dielectric Screening in Atomically Thin Boron Nitride Nanosheets. *Nano Letters*

        2015, *15* (1), 218-223.

55.   Li, L. H.; Tian, T.; Cai, Q.; Shih, C.-J.; Santos, E. J. G., Asymmetric electric field screening in

        van der Waals heterostructures. *Nature Communications* **2018,** *9* (1), 1271.

56.   Su, R.; Xu, Z.; Wu, J.; Luo, D.; Hu, Q.; Yang, W.; Yang, X.; Zhang, R.; Yu, H.; Russell, T. P.;

        Gong, Q.; Zhang, W.; Zhu, R., Dielectric screening in perovskite photovoltaics. *Nature*

        Communications **2021,** *12* (1), 2479.

57.   Safa Kasap, P. C., *Springer Handbook of Electronic and Photonic Materials*. Springer: 2017.

58.   Miller, E. M.; Zhao, Y.; Mercado, C. C.; Saha, S. K.; Luther, J. M.; Zhu, K.; Stevanović, V.;

        Perkins, C. L.; van de Lagemaat, J., Substrate-controlled band positions in CH3NH3PbI3

        perovskite films. *Physical Chemistry Chemical Physics* **2014,** *16* (40), 22122-22130.

59.   Mao, L.; Stoumpos, C. C.; Kanatzidis, M. G., Two-Dimensional Hybrid Halide Perovskites:

        Principles and Promises. *Journal of the American Chemical Society* **2019,** *141* (3), 1171-1190.

60. Liam Collins, E. S. M., Hsinhan Tsai, Dibyajyoti Ghosh, Amanda J. Neukirch, Sergei Tretiak, Sergei V. Kalinin, Wanyi Nie, Ilia N. Ivanov Correlation of Spatiotemporal Dynamics of Polarization and Charge Transport in Blended Hybrid Organic−Inorganic Perovskites on Macro- and Nanoscales. *ACS Applied Materials and Interfaces* **2020,** *12*, 15380-15388.

61. Spanopoulos, I.; Hadar, I.; Ke, W.; Tu, Q.; Chen, M.; Tsai, H.; He, Y.; Shekhawat, G.; Dravid, V. P.; Wasielewski, M. R.; Mohite, A. D.; Stoumpos, C. C.; Kanatzidis, M. G., Uniaxial Expansion of the 2D Ruddlesden–Popper Perovskite Family for Improved Environmental Stability. *Journal of the American Chemical Society* **2019,** *141* (13), 5518-5534.

62. Zhao, Y.-Q.; Ma, Q.-R.; Liu, B.; Yu, Z.-L.; Yang, J.; Cai, M.-Q., Layer-dependent transport and optoelectronic property in two-dimensional perovskite: (PEA)2PbI4. *Nanoscale* **2018,** *10* (18), 8677-8688.